RILEM Technical Letters (2021) 6: 169-187, Supplementary material
https://doi.org/10.21809/rilemtechlett.2021.151

Supplementary material
Alkali-silica reaction – a multidisciplinary approach

Andreas Leemann[1], Mahsa Bagheri[2], Barbara Lothenbach[1], Karen Scrivener[2], Solène Barbotin[2], Emmanuelle Boehm-Courjault[2], Guoqing Geng[3,4], Rainer Dähn[3], Zhenguo Shi[1,5], Mahdieh Shakoorioskooie[1,6,7], Michele Griffa[1], Robert Zboray[6], Pietro Lura[1,7], Emil Gallyamov[8], Roozbeh Rezakhani[8,9], Jean-Francois Molinari[8]

[1] Concrete and Asphalt Laboratory, Empa, Swiss Federal Laboratories for Materials Science and Technology, 8600 Dübendorf, Switzerland
[2] Materials Institute, Laboratory of Construction Materials, EPFL, 1015 Lausanne, Switzerland
[3] Laboratory for Waste Management, Paul Scherrer Institute, 5232Villigen PSI, Switzerland
[4] National University of Singapore, Department of Civil & Environmental Engineering, Engineering Drive 2, Singapore 117576
[5] Present address: Global R&D, HeidelbergCement AG, Oberklamweg 2-4, 69181 Leimen, Germany
[6] Center for X-ray Analytics, Empa, Swiss Federal Laboratories for Materials Science and Technology, 8600, Dübendorf, Switzerland
[7] Institute for Building Materials (IfB), ETH Zürich, 8093, Zürich, Switzerland
[8] Civil Engineering Institute, Materials Science and Engineering Institute, EPF Lausanne, Station 18, 1015 Lausanne, Switzerland
[9] Department of Mechanical Engineering and Material Science, Duke University, Durham, NC, USA

Received: 17 November 2021 / Accepted: 13 February 2022 / Published online: 28 March 2022
© The Author(s) 2022. This article is published with open access and licensed under a Creative Commons Attribution 4.0 International License.

S1. Subproject I: Materials and methods

S1.1. Scratch-tracking method

The scratch tacking method has been used to identify which minerals in a composite aggregate are most susceptible to ASR using a reactive Alpine aggregate from Praz in Switzerland (P aggregate, gneiss/quartzite). Table 1 shows XRD and XRF results, indicating that P aggregate contains almost 56 wt. % of quartz (SiO_2), 8 wt. % of potassium ($KAlSi_3O_8$) and 8 wt. % of sodium feldspars ($NaAlSi_3O_8$). In a first step, aggregates with size fraction of 1-2 cm were impregnated with epoxy and polished. SEM images of the polished surface were collected from identical locations before and after 21 and 60 days of dissolution in 0.4M KOH solution at 38 °C. The extent of dissolution was quantified based on aligned SEM images of the same areas as further detailed in [1]. Based on the area occupied by the scratches before and after dissolution, the increase of the scratch surface area fraction (ΔSSAF (%) is calculated [1,2].

S1.2. Solution analysis

The dissolution rates of amorphous silica (synthetic silica powders), quartz, K-feldspar and Na-feldspar were studied in the presence of different ions (such as Al (0.1 - 3 mM), Fe, Mg and Ca (3 mM), Li (10 – 400 mM), Na, K and Cs (400 mM) and sulfate (50 and 200 mM)) at high pH values in aqueous solution [2]. The increase of Si concentrations with time was measured in highly diluted samples (liquid to solid ratio = 500 mL to 0.5 g) at 20, 40 and 60 °C. The concentration of Si released from the solids was measured using Inductively Coupled Plasma Optical Emission Spectrometry (ICP-OES) or Ion Chromatography (IC) in small aliquots of the solution, and the slope of the Si concentration as a function of time was used to fit the Si release rate as detailed in [2].

S2. Subproject II: Materials & Method

For the concrete samples produced in the lab and exposed to accelerated conditions, five batches were prepared with P aggregate (Table 1). 1770 kg/m^3 of aggregates were used with a maximum aggregate size of 22.4 mm. Binder content was 400 kg/m^3 with a water-to-binder ratio of 0.46. The binder used and their relative proportions in mass-% are given in Table 2 and the composition in Table 3.

The samples were cast in moulds of 70×70×281 mm^3. After demolding at 24h, the prisms were stored in water vapour (WV) at 60°C (T60) according to the Swiss standard SIA 262-1 [3]. After 2 and 4 weeks (PC), and 20 weeks (PC+FA and PC+LC^3) in accelerated conditions, samples from the prisms were taken, dried for 3 days in air at 40°C, impregnated with epoxy and polished according to method specified in [4].

* Corresponding author: Andreas Leemann, E-mail: andreas.leemann@empa.ch

Table 1. Chemical and mineralogical composition of the P aggregate, reproduced from [1]

Technique	Component	P
XRF (wt. %)	SiO_2	68.0
	Al_2O_3	7.2
	CaO	8.9
	K_2O	2.2
	MgO	1.9
	Fe_2O_3	1.4
	Na_2O	1.4
	SO_3	0.1
XRD (wt. %)	**Quartz**: SiO_2 [ICSD 174]	55.5
	Feldspar: Albite: $NaAlSi_3O_8$ [ICSD 87657]	8.2
	Feldspar: Microcline: $KAlSi_3O_8$ [ICSD 83531]	7.9
	Mica: Muscovite: $KAl_2(AlSi_3O_{10})(OH)_2$ [ICSD 75952]	7.4
	Calcite: $CaCO_3$ [ICSD 73446]	15.2
	Dolomite: $CaMg(CO_3)_2$ [ICSD 66333]	4.5
	Amorphous/non-crystalline	1.3

Table 2. Binder proportions for each concrete mix.

In mass-%	Cement	Siliceous FA	Calcined Clay	Limestone	$Na_2O_{Eq.}$
OPC	100	0	0	0	0.83
FA	70	30	0	0	0.77
LC[3]	55	0	30	15	0.57
LC[3 1]	55	0	30	15	0.80
LC[3 2]	55	0	30	15	1.25

[1] boosted with NaOH to reach a Na_2Oeq of 0.80 mass-%
[2] boosted with NaOH to reach a Na_2Oeq of 1.25 mass-%

Table 3. XRF results of the raw materials used to produce the concrete in mass-%. LOI: loss of ignition.

	Limestone	Calcined clay	Fly Ash	PC
SiO_2	0.11	49.74	50.54	20.45
Al_2O_3	0.00	41.78	24.70	4.39
Fe_2O_3	0.04	2.30	9.29	3.01
CaO	54.96	0.20	5.07	64.48
MgO	0.20	0.10	2.88	1.66
SO_3	0.03	0.00	0.71	2.83
Na_2O	0.06	0.30	1.05	0.24
K_2O	0.01	0.10	4.10	0.89
TiO_2	0.01	3.40	0.95	0.34
P_2O_5	0.00	0.09	0.00	0.28
MnO	0.00	0.02	0.00	0.06
Others	0.00	0.00	0.00	0.10
LOI	42.60	1.85	0.71	1.30
Na_2O eq	0.06	0.37	3.75	0.83

Samples from the field (PC concrete) were also taken and prepared in the same way. Using a SEM, various area of interest were localized, according to the following criteria:

- Located in the aggregate, a minimum of 100 µm away from the cement-aggregate interface
- Located between adjacent quartz grains

The area of interest, cracks containing ASR product, were then cut with a FIB and later analyzed in a TEM in STEM mode and additionally performing selected area electron diffraction (SAED) according to [4].

S3. Subproject III: Materials and methods

S3.1. Materials

In subproject III, samples from both ASR-damaged concrete (field samples) and laboratory-synthesis were studied. Details can be found in our published work [5-7]. In brief, Mels1, ES1 and ES2 are from naturally damaged concrete in Mels (Switzerland), Valencia (Spain) and Milan (Italy), respectively. 'N1' was obtained from a concrete subjected to the Norwegian 38 °C prism test for two years. For 3D tomographic XRD study, a sub-volume containing an ASR product vein was extracted from ES1 using focused ion beam (FIB). Reference minerals mountainite and shlykovite were obtained from a Russian mineralogy research group. SKC and SNC are shlykovite-type samples synthesized by subproject IV at 80 ℃ for three months [8]. A calcium-silicate-hydrates (C-S-H) sample with significant K uptake was also studied, denoted as K_CSH.

S3.2. Methods

2D Micro-XAS study was conducted at the *PHOENIX beamline* of the Swiss Light Source (SLS) using settings given in [5]. The XAS at Ca, K and Na *K*-edge were obtained at the locations of interest and analyzed using the Athena package.

3D tomographic micro-XRD study was conducted at the *microXAS beamline* of the SLS with details given in [9]. The sample was subjected to R.H. varied from 10% (dry), 38% (ambient) to 97% (wet). At each R.H. the XRD scan was conducted at every 1.6° angle over a full rotation angle of 180°. The full rotation was conducted at several consecutive vertical positions of the sample. Reconstructions were conducted with both florescence signal and intensities of selected XRD peaks, using the Astra Toolbox library based on simultaneous iterative reconstruction technique (SIRT) [10].

S4. Subproject IV: Materials and methods

S4.1. Materials

Various types of ASR products were synthesized at 20, 40, 60, and 80°C by mixing amorphous silica (hydrophilic silica (SiO_2), surface area 200 m^2/g, from EVONIK industries) with freshly burnt CaO (obtained by burning calcium carbonate for 12 h at 1000 °C) and NaOH and/or KOH pellets at designated portions. Samples with different K/Na ratios (0, 1.0, 2.3, and 6.1) and Na/K ratio of 0 were prepared with a constant molar (K + Na)/Si ratio of 0.5 and Ca/Si ratio of 0.25 as reported in previous studies [8, 11-15].

S4.2. Methods

The synthetic ASR products are characterized using various laboratory techniques, such as SEM/EDX, TGA, XRD, FTIR, NMR, Raman and DVS [8, 11-15]. For comparison, ASR products formed in concrete were also characterized. However, due to the small amounts of ASR products formed in concrete aggregates, these ASR products are mainly characterized at micro-scale using SEM/EDX and Raman spectroscopy. In a few cases, where sufficient amounts (a few mg) of ASR products were sampled from ASR-affected concretes, the ASR products are also characterized with capillary XRD and DVS methods. These data are compared with those of synthetic ASR products to confirm the representativeness of ASR products synthesized in the laboratory [16,17].

S5. Subproject V: Materials, methods and multimedia results

S5.1. Materials

The results reported in this work were obtained for 40×40×160 mm^3 concrete specimens cast with the U aggregate. It is mainly constituted of micro-crystalline quartz, including small amounts of amorphous SiO_2 (mainly in the form of detrital chert fragments and siliceous inclusions in the cementing intergranular regions), feldspar and calcite [18]. The maximum aggregate sieve size was 11.2 mm. 1647 kg/m^3 of aggregates and 450 kg/m^3 of PC (Table 3) at a w/c of 0.50 were used for concrete production [19]. Inert $BaSO_4$ [20] was added in the amount of 43 kg/m^3. Additionally, 13.6 kg/m^3 of $CsNO_3$ was added. Cs is incorporated into the ASR products [21]. It increased their X-ray attenuation well above that of the other material phases [19]. The cast specimens were immersed into an alkaline solution (0.3 M KOH, 0.1 M NaOH) and stored in an oven at 40 °C, except at the measurement times.

S5.2. Methods

We performed XT using a lab-based, cone-beam micro-focus tomograph, operated at a maximum photon energy of 90 keV. The spatial resolution of the tomograms (~ two times the voxel size) was 70 μm. The segmentation of the aggregates from the paste was achieved by simple voxel value range selection (thresholding), thanks to the $BaSO_4$-enhanced contrast between paste and aggregates. The binary tomograms of segmented aggregates and paste allowed quantifying features of cracks and products, while differentiating between their presence in each solid phase.

A customized workflow was developed and implemented to minimize human choices in the more challenging segmentation of cracks and products. Such workflow relied on an approach known as Temporal Subtraction (TS), frequently used in the biomedical imaging community [22] but less exploited in the porous materials one. Details of such approach are available in [19].

We used several algorithms/approaches to characterize quantitatively the products and the cracks, with the novelty of contextualizing the characterization (inside aggregates or

paste). The details of all the image analysis workflows are provided in [19].

S5.3. Qualitative analysis of ASR products accumulation and cracking using time-lapse X-ray tomography

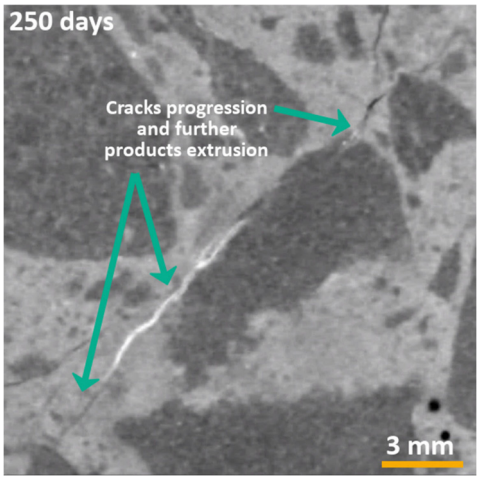

Movie MS1. This movie shows the time series of the same region of interest (ROI) extracted from the time-lapse tomograms of a specimen cast with Uri aggregates and with $BaSO_4$ and $CsNO_3$ as contrast enhancers. Only a 2D cross-section ("slice") from the ROI is shown, at the same position at any time point. The last frame of the movie is shown above. The time series of the "non-affinely" registered tomograms was used for producing this movie. This allowed full sequential comparability of the slice at distinct time points, since the misalignment and specimen deformations were corrected for. The time points (from 1 day to 250 days) at which the slices were selected are specified over each corresponding slice. The ROI considered in this movie corresponds to the same one used for Figure 15 in the main article. The movie file is called **Movie_MS1.avi** and is available at https://doi.org/10.5281/zenodo.5913693.

S6. Subproject VI: Methods

S6.1. Meso-scale

Tomography data of concrete specimens provided by the colleagues from EMPA is used to set up three-dimensional finite-element model. Intact laboratory specimens of concrete are transformed into finite element models and later used to advance ASR (see **Error! Reference source not found.**1). ASR-sites were modelled by pairs of opposite direction point loads applied at the interfaces between solid finite elements, which represent pressure of expanding ASR products.

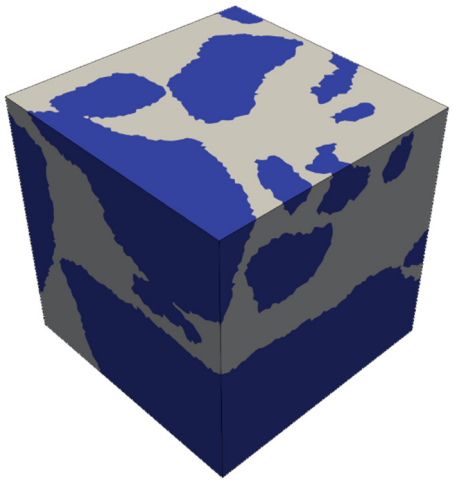

Figure 1. Irregular finite element mesh created from tomography data provided by Subproject V.

S6.2. Macro-scale

In order to obtain the solution at the macroscopic scale, one has to resolve stresses at each integration point. For this purpose, the deformation gradients $\bar{F}$ are collected at the macro-scale and imposed at the meso-scale in the form of boundary conditions. The deformation applied at the RVE together with the internal pressure from the ASR pockets forces the meso-scale problem to evolve. This evolution manifests as purely elastic deformations or crack initiation and growth. Stresses homogenized over an RVE, $\bar{\sigma}$, are passed to the macro-scale where they are integrated into the internal force vector. If convergence is achieved, the simulation proceeds to the next loading step. If not, the macroscopic displacement field is recomputed with the help of the macroscopic stiffness matrix. The latter is built from the homogenized stiffness tensors of meso-scale RVEs, $\bar{\mathbb{C}}$. More details can be found in [23].

References

[1] M. Bagheri, B. Lothenbach, M. Shakoorioskooie, A. Leemann, K. Scrivener, Use of scratch tracking method to study the dissolution of alpine aggregates subject to alkali silica reaction. Cem Concr Compos (2021) 124: 104260. https://doi.org/10.1016/j.cemconcomp.2021.104260

[2] M. Bagheri, B. Lothenbach, M. Shakoorioskooie, K. Scrivener, Effect of different ions on dissolution rates of silica and feldspars at high pH. Cem Concr Res (2022) 152:106644. https://doi.org/10.1016/j.cemconres.2021.106644.

[3] SIA 262-1, Construction en béton - Spécifications complémentaires, Appendice G. SIA Zurich (2019).

[4] E. Boehm-Courjault, S. Barbotin, A. Leemann, K. Scrivener, Microstructure, crystallinity and composition of alkali-silica reaction products in concrete determined by transmission electron microscopy. Cem Concr Res (2020) 130:105988. https://doi.org/10.1016/j.cemconres.2020.105988.

[5] G. Geng, Z. Shi, A. Leemann, C. Borca, T. Huthwelker, K. Glazyrin, I.V. Pekov, S. Churakov, B. Lothenbach, R. Dähn, E. Wieland, Atomistic structure of alkali-silica reaction products refined from X-ray diffraction and micro X-ray absorption data. Cem Concr Res (2020) 129:105958. https://doi.org/10.1016/j.cemconres.2019.105958.

[6] G. Geng, Z. Shi, A. Leemann, K. Glazyrin, A. Kleppe, D. Daisenberger, S. Churakov, B. Lothenbach, E. Wieland, R. Dähn, Mechanical behavior and phase change of alkali-silica reaction products under hydrostatic compression. Acta Crystallogr B (2020) 76(4). https://doi.org/10.1107/S205252062000846X.

[7] G. Geng, S. Barbotin, M. Shakoorioskooie, Z. Shi, A. Leemann, D.F. Sanchez, D. Grolimund, E. Wieland, R. Dähn, An in-situ 3D micro-XRD investigation of water uptake by alkali-silica-reaction (ASR) product. Cem Concr Res (2021) 141:106331. https://doi.org/10.1016/j.cemconres.2020.106331.
[8] Z. Shi, G. Geng, A. Leemann, B. Lothenbach, Synthesis, characterization, and water uptake property of alkali-silica reaction products. Cem Concr Res (2019) 121:58–71. https://doi.rog/10.1016/j.cemconres.2019.04.009.
[9] C.N. Borca, D. Grolimund, M. Willimann, B. Meyer, K. Jefimovs, J. Vila-Comamala, C. David, The microXAS beamline at the Swiss Light source: towards nano-scale imaging. J Physics: Conference Series (2009) 186(1):12003. https://doi.org/10.1088/1742-6596/186/1/012003.
[10] W. van Aarle, W.J. Palenstijn, J. Cant, E. Janssens, F. Bleichrodt, A. Dabravolski, J. De Beenhouwer, K. J. Batenburg, J. Sijbers, Fast and flexible x-ray tomography using the ASTRA Toolbox. Opt. Express (2016) 24(22):25129-25147.
[11] Z. Shi, A. Leemann, D. Rentsch, B. Lothenbach, Synthesis of alkali-silica reaction product structurally identical to that formed in field concrete. Mater Design (2020) 190:108562. https://doi.org/10.1016/j.matdes.2020.108562.
[12] Z. Shi, G. Geng, A. Leemann, B. Lothenbach, Synthesis, characterization, and water uptake property of alkali-silica reaction products. Cem Concr Res (2019) 121:58–71. https://doi.org/10.1016/j.cemconres.2019.04.009
[13] Z. Shi, B. Lothenbach, The combined effect of potassium, sodium and calcium on the formation of alkali-silica reaction products. Cem Concr Res (2020) 127:105914. https://doi.org/10.1016/j.cemconres.2019.105914.
[14] Z. Shi, B. Lothenbach, The role of calcium on the formation of alkali-silica reaction products. Cem Concr Res (2019) 126. 105898. https://doi.org/10.1016/j.cemconres.2019.105898.
[15] Z. Shi, B. Ma, B. Lothenbach, Effect of Al on the formation and structure of alkali-silica reaction products. Cem Concr Res (2021) 140:106311. https://doi.org/10.1016/j.cemconres.2020.106311.
[16] Z. Shi, S. Park, B. Lothenbach, A. Leemann, Formation of shlykovite and ASR-P1 in concrete under accelerated alkali-silica reaction at 60 and 80° C. Cem Concr Res (2020) 137:106213. https://doi.org/10.1016/j.cemconres.2020.106213.
[17] A. Leemann, Z. Shi, J. Lindgård, Characterization of amorphous and crystalline ASR products formed in concrete aggregates. Cem Concr Res (2020) 137:106190. https://doi.org/10.1016/j.cemconres.2020.106190.
[18] C. Bärtschi, Kieselkalke der Schweiz: Charakterisierung eines Rohstoffs aus geologischer, petrographischer, wirtschaftlicher und umweltrelevanter Sicht. PhD Thesis, ETH Zurich, 2011. https://doi.org/10.3929/ETHZ-A-006471191.
[19] M. Shakoorioskooie, M. Griffa, A. Leemann, R. Zboray, P. Lura, Alkali-silica reaction products and cracks: X-ray micro-tomography-based analysis of their spatial-temporal evolution at a mesoscale. Cem Concr Res (2021) 150:106593. https://doi.org/10.1016/j.cemconres.2021.106593.
[20] P. Carrara, R. Kruse, D.P. Bentz, M. Lunardelli, T. Leusmann, P.A. Varady, L. De Lorenzis, Improved mesoscale segmentation of concrete from 3D X-ray images using contrast enhancers. Cem Concr Compos (2018) 93:30–42. https://doi.org/10.1016/j.cemconcomp.2018.06.014.
[21] A. Leemann, B. Münch, The addition of caesium to concrete with alkali-silica reaction: Implications on product identification and recognition of the reaction sequence. Cem Concr Res (2019) 120: 27-35. https://doi.org/10.1016/j.cemconres.2019.03.016.
[22] R. Sakamoto, M. Yakami, K. Fujimoto, K. Nakagomi, T. Kubo, Y. Emoto, T, Akasaka, G. Aoyama, H. Yamamoto, M.I. Miller, S. Mori, K. Togashi, Temporal subtraction of serial CT images with large deformation diffeomorphic metric mapping in the identification of bone metastases. *Radiology* (2017) *285*(2):629-639. https://doi.org/10.1148/radiol.2017161942
[23] E.R. Gallyamov, A.I. Cuba Ramos, M. Corrado, R. Rezakhani, J.-F. Molinari, Multi-scale modelling of concrete structures affected by alkali-silica reaction: Coupling the mesoscopic damage evolution and the macroscopic concrete deterioration. Int J Solids Struct (2020) 207:262-278. https://doi.org/10.1016/j.ijsolstr.2020.10.010.